

Sensitivity analysis of seismic waveforms to upper-mantle discontinuities using the adjoint method

Maria Koroni,¹ Ebru Bozdağ,² Hanneke Paulssen¹ and Jeannot Trampert¹

¹*Department of Earth Sciences, Universiteit Utrecht, Heidelberglaan 2, NL-3584 CS Utrecht, The Netherlands. E-mail: m.koroni@uu.nl*

²*Department of Geophysics, Colorado School of Mines, 1500 Illinois Street, Golden, CO 80401, USA*

Accepted 2017 July 4. Received 2017 July 3; in original form 2017 April 10

SUMMARY

Using spectral-element simulations of wave propagation, we investigated the sensitivity of seismic waveforms, recorded on transverse components, to upper-mantle discontinuities in 1-D and 3-D background models. These sensitivity kernels, or Fréchet derivatives, illustrate the spatial sensitivity to model parameters, of which those for shear wave speed and the surface topography of internal boundaries are discussed in this paper. We focus on the boundaries at 400 and 670 km depth of the mantle transition zone. *SS* precursors have frequently been used to infer the topography of upper-mantle discontinuities. These seismic phases are underside reflections off these boundaries and are usually analysed in the distance range of 110°–160°. This distance range is chosen to minimize the interference from other waves. We show sensitivity kernels for consecutive time windows at three characteristic epicentral distances within the 110°–160° range. The sensitivity kernels are computed with the adjoint method using synthetic data. From our simulations we can draw three main conclusions: (i) The exact Fréchet derivatives show that in all time windows, and also in those centred on the *SS* precursors, there is interference from other waves. This explains the difficulty reported in the literature to correct for 3-D shear wave speed perturbations, even if the 3-D structure is perfectly known. (ii) All studies attempting to map the topography of the 400 and 670 km discontinuities to date assume that the traveltimes of *SS* precursors can be linearly decomposed into a 3-D elastic structure and a topography part. We recently showed that such a linear decomposition is not possible for *SS* precursors, and the sensitivity kernels presented in this paper explain why. (iii) In agreement with previous work, we show that other parts of the seismograms have greater sensitivity to upper-mantle discontinuities than *SS* precursors, especially multiply bouncing *S* waves exploiting the *S*-wave triplications due to the mantle transition zone. These phases can potentially improve the inference of global topographic variations of the upper-mantle discontinuities in the context of full waveform inversion in a joint inversion for (an)elastic parameters and topography.

Key words: Body waves; Computational seismology; Wave propagation.

1 INTRODUCTION

In the scientific community, the consensus is that upper-mantle discontinuities are most likely caused by phase changes of mantle minerals and are found around depths of 410 and 660 km (e.g. Revenaugh & Jordan 1991; Shearer 1991; Deuss 2009). We will refer to them as occurring at 400 and 670 km because in this paper we only present evidence from a synthetic study, which uses PREM (Dziewoński & Anderson 1981) as a background model. In PREM, the discontinuities are fixed at depths of 400 and 670 km, and this is the naming we adopt here. These discontinuities were first discovered using array studies (Niazi & Anderson 1965; Johnson 1967)

in which the triplication of body waves caused by the upper-mantle discontinuities in the distance range 15°–30° was exploited. These triplications were further used in waveform modelling studies (e.g. Grand & Helmberger 1984; Tan & Helmberger 2007; Staelher *et al.* 2012) to more tightly constrain the nature of the transition zone discontinuities. However, to the best of our knowledge, they have not been exploited for the global mapping of discontinuity topography. The lateral resolution of these studies is usually low and confined to the corridor of the event connecting the array (Zhao & Helmberger 1993). Receiver functions have also been used to identify upper-mantle discontinuities (Vinnik 1977). This type of study samples the mantle structure directly beneath seismic stations

and can thus result in high lateral resolution, provided the station distribution is dense (e.g. Rondenay 2009). The downside of the receiver function studies is that the access to the upper-mantle discontinuities is restricted beneath continents, where the stations are usually located. Precursors to surface reflected phases (*SS* and to a lesser extent *PP*) have proven to be much better at resolving the nature of upper-mantle discontinuities globally. These precursors follow a similar path to that of the *SS* wave, but instead of being reflected at the free surface, they are reflected at the underside of the discontinuities. The precursors arrive 2–4 min before the *SS* wave. The reason for using them is that they are thought to be mainly sensitive to the structure beneath the bounce points (halfway between source and receiver great circle path) and hence allow us to sample oceanic as well as continental regions. For an overview the reader is referred to Deuss (2009). In a different approach, Meier *et al.* (2009) used surface wave overtones to infer the global structure of the mantle transition zone.

It is important to understand the seismic structure around 400 km and 670 km depth because it puts strong constraints on the temperature and composition at the boundaries of the upper mantle transition zone (e.g. Helffrich 1999; Shearer 2000; Schmerr & Garnero 2006; Deuss 2009) and hence the geodynamic nature of the mantle. Much effort has been dedicated to inferring the topographic variations of the mantle transition zone discontinuities using observations of *SS* precursors together with ray theory (e.g. Shearer 1991, 1993, 2000; Shearer & Masters 1992; Flanagan & Shearer 1998, 1999; Gu & Dziewonski 1998; Gu & Dziewonski 2002; Gu *et al.* 2003; Chambers *et al.* 2005; Schmerr & Garnero 2006; Houser *et al.* 2008; Lawrence & Shearer 2008). Despite an intense research effort, many discrepancies between the studies remain, which are currently not completely understood. The problem is similar or even worse for *PP* precursors, but we will not address the *PP* phases any further here. The traveltimes of the *SS* precursors do not only depend on the topography of the discontinuities, but also on the 3-D velocity structure of the mantle. A correction of the latter therefore needs to be applied to the observed traveltimes, and this is a likely cause of the discrepancies between the studies. Indeed, Bai *et al.* (2012) showed that even if the 3-D structure is perfectly known, ray theory can only explain about 50 per cent of the traveltime anomalies produced by it. The complicated shape of the Fresnel zones associated with minimax phases has been put forward to explain the problem with traveltime corrections (Chaljub & Tarantola 1997; Zhao & Chevrot 2003). Recently, Koroni & Trampert (2016) have identified a more fundamental problem, that *SS* traveltimes cannot be linearly decomposed into a 3-D velocity structure and a discontinuity topography part.

In this study, we analysed finite frequency kernels to understand what causes the problems associated with inferring mantle transition zone structure from traveltimes of *SS* precursors. We calculated exact seismograms in 1-D and 3-D background models and added topography to the upper-mantle discontinuities. The study is entirely synthetic. Analysing the evidence based on finite frequency kernels, we found that within the precursor window there is always interference of several seismic waves. This explains why a correction based on a single wave cannot properly account for the 3-D seismic structure. We also found that the sensitivity of the traveltimes of *SS* precursors to the boundary denoting the discontinuity changes significantly with the background model. We argue that this is the reason why effects of 3-D velocity structure and topography are not additive for a given traveltime anomaly. In agreement with other studies, we identified areas in the seismogram, associated with multiply bouncing *S* waves, that are far more sensitive to the upper-

mantle discontinuities than *SS* precursors, which to our knowledge have never been used for a global mapping of the discontinuities. In the following, the methods for computing the sensitivity kernels will be described. We will show the resulting volumetric and boundary sensitivity kernels. Lastly, we will discuss our results and analyse their implications regarding the inference of topography of upper-mantle discontinuities.

2 SYNTHETIC DATA AND CALCULATION OF THE SENSITIVITY KERNELS

To investigate the sensitivity of the waveforms and especially of the *SS* precursors, we used part of the data generated in Koroni & Trampert (2016) and a detailed description of it can be found in their paragraph 2.1. We used both 1-D and 3-D elastic models for the simulations of the synthetic data. The 1-D background model is PREM (Dziewoński & Anderson 1981) and is used for the calculations of most of the sensitivity kernels, the 3-D mantle model is S20RTS (Ritsema *et al.* 1999) combined with the CRUST2.0 (Bassin *et al.* 2000) and the topography models are from Meier *et al.* (2009) scaled to ± 30 km. The models are used to study the effects of 3-D shear velocity and topographic perturbations on *SS* precursors signals. We used 1-hr long transverse component seismograms and PREM arrival times to select the time windows and to calculate the Fréchet derivatives (or sensitivity kernels). The earthquake source is a pure strike-slip event of magnitude 7.9 at a depth of 20 km. The source time function (STF) is set to a Gaussian of half-width equal to 30 s and the resolution of the seismograms is such that they are accurate down to a minimum period of 18 s. We use the STF to smooth the kernels which otherwise would appear oscillatory and it would be harder to identify the various phases. The STF is twice as large as what would be expected for an event of magnitude 7.9 (Ekström *et al.* 2012) still our seismograms have dominant amplitudes in the period range 30–150 s, the high frequency band being close to the periods often used in *SS* precursor studies. For a single source, at the equator at 300° longitude, we selected 3 receivers as shown in Fig. 1 at epicentral distances of approximately 110° , 140° and 160° . These three distances show the main characteristics of the sensitivity kernels as illustrated in the next section. The simulations were done with the spectral element package SPECFEM3D_GLOBE (Komatitsch & Vilotte 1998; Komatitsch & Tromp 1999, 2002a,b).

The calculation of the Fréchet derivatives is based on adjoint methods. For a review of adjoint methods in geophysical problems, the reader is referred to Tarantola (1984), Gauthier *et al.* (1986), Talagrand & Courtier (1987) and Tarantola (1988). The mathematics of our implementation is developed in the papers of Tromp *et al.* (2005); Liu & Tromp (2006, 2008) and coded up in the numerical package SPECFEM3D_GLOBE, the same code we used for the calculation of the synthetic data and sensitivity kernels. Prior to the calculation of the sensitivity kernels, the synthetic data were processed in the following way: we removed the mean, tapered and filtered them using a band-pass with corners at 22 and 250 s. We selected narrow time windows on the transverse component waveforms to investigate the sensitivity of seismic phases. The variable time windows (see Tables 1–3) are 20 per cent cosine tapered centred around the arrival time we want to investigate.

The first step towards the computation of the Fréchet derivatives is to define an objective or misfit function. For simplicity we only show sensitivity kernels for traveltime anomalies measured by cross-correlation (e.g. Luo & Schuster 1991; Marquering

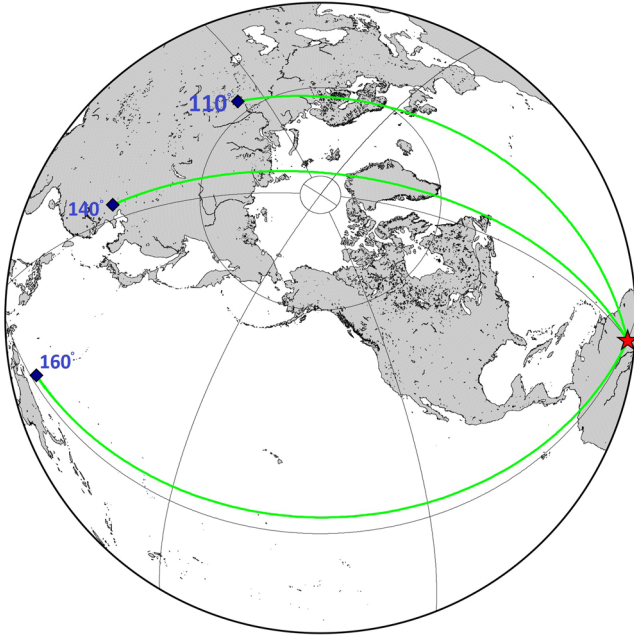


Figure 1. The source (red star) and receiver (blue diamonds) configuration. The stations are at epicentral distances of 110.84°, 143.04° and 160.58°.

et al. 1999; Dahlen *et al.* 2000). These are sometimes referred to as banana-doughnut kernels (e.g. Marquering *et al.* 1999; Dahlen *et al.* 2000). The reader is referred to Tromp *et al.* (2005) for a complete derivation of the expressions relating the traveltime to the sensitivity kernels, which are used here. Below we will only show sensitivity kernels with respect to a relative shear wave speed perturbation in the model volume and to a relative topography perturbation at the surface of the internal boundaries. The traveltime sensitivity kernels are defined by the following expressions:

$$\delta t = \int_V K_{V_{SH}} \delta \ln V_{SH} d^3x \quad (1)$$

and

$$\delta t = \int_S K_r \delta \ln r d^2x \quad (2)$$

where, $\delta \ln V_{SH}$ is the relative shear wave speed perturbation and $\delta \ln r$ denotes the relative perturbation of the radius of the discontinuity. δt is the traveltime anomaly due to a relative perturbation in shear wave speed or the radius of the discontinuity multiplied by the kernel integrated over the volume V , for a volumetric kernel, or the surface S , for a boundary kernel, respectively. The units for $K_{V_{SH}}$ are thus in $[s \text{ km}^{-3}]$ and for K_r in $[s \text{ km}^{-2}]$. All kernels are shown without having been processed in any way, besides the implicit smoothing via the STF. Note that in actual tomographic inversions, kernels are usually smoothed further. The volumetric shear wave speed kernels are shown by taking cross-sections cut along the great circle path connecting source and receiver. The boundary kernels are shown in lateral sections at the surface of the boundaries located at 400 and 670 km depths in PREM.

3 A GALLERY OF SENSITIVITY KERNELS

In this section, we show volumetric and boundary kernels for the three epicentral distances (110°, 140° and 160°) calculated in the background model PREM. For the distance of 140°, we also show

boundary kernels in the 3-D model S20RTS plus CRUST2.0 (from now on denoted by S20RTS) to compare them to those in PREM. The time windows for each kernel are shown together with the corresponding transverse component seismogram. We use the naming convention of the TauP software (Crotwell *et al.* 1999) to identify phases seen on the sensitivity kernels. In what follows, the symbol \wedge denotes an underside reflection, while the symbol \vee denotes a top-side reflection off the depth of the discontinuity.

3.1 110° distance

The Fréchet derivatives representing the sensitivity to relative volumetric changes in V_{SH} are shown in Fig. 2 and the ray theoretical arrivals, calculated by TauP are shown in Table 1 per time window. Time window (a) corresponds to a kernel which shows a pure sensitivity to S_{diff} in the shape of a banana-doughnut kernel. We see no clear sign of the core phases theoretically arriving in the same time window. Time window (b) is mainly sensitive to S_{diff} . Its sensitivity kernel shows higher order Fresnel zones of S_{diff} sensitivity because the time window is in the coda of S_{diff} and there are possible reverberations in D'' . D'' is a second order discontinuity at 150 km above the core-mantle boundary in PREM, which has been used for the calculation of the sensitivity kernels. PREM also contains a first order discontinuity at a depth of 220 km. Therefore, top-side reflections of S_{diff} off the 220 km discontinuity ($S\vee 220sS_{\text{diff}}$ and $S_{\text{diff}}S\vee 220s$) arrive in this time window, and as a consequence there is a hint of their sensitivity in the kernel. Time window (c) contains a 400 km top-side reflection of S_{diff} and a double top-side reflection at the 220 km discontinuity, and hence the kernel is that of S_{diff} with symmetric reflection legs. The reflections off the 220 and 400 km discontinuities interfere and are therefore only faintly visible. The underside reflection of the SS wave at the 670 km discontinuity arrives in window (d). The arrival of the $S\wedge 670S$ phase almost coincides with the top-side reflection of S_{diff} at the same discontinuity. Therefore the kernel has a sensitivity to S_{diff} besides the 670 km precursor of SS . The top-side reflection legs appear symmetric because $S\vee 670sS_{\text{diff}}$ arrives at the same time as $S_{\text{diff}}S\vee 670s$. There is also some interference with $S\vee 220sS_{\text{diff}}S\vee 220s$. Time window (e) corresponds to the arrival of the 400 km precursor to SS , but the sensitivity kernel also shows the higher order Fresnel zones of the S_{diff} top-side reflection at the same discontinuity ($S\vee 400sS_{\text{diff}}S\vee 400s$). Note that due to the source time function of 60 s, 670-related waves also arrive in this time window, but they are difficult to identify due to the overall complexity of the kernel. Time window (f) is that of the underside reflection of SS at the 220 km discontinuity. Because of the source time function in our simulations, SS starts to arrive in this time window and we still observe the imprint of $S\vee 400sS_{\text{diff}}S\vee 400s$. Time window (g) mainly contains SS , but again due to our source time function, the effect of $S\vee 670sSS\vee 670s$ can also be seen. It is interesting to note that no time window contains a pure precursory phase, but each time window contains multiple arrivals. If we looked at horizontal slices of the volumetric kernels at the depths of the discontinuities rather than vertical slices along the great circle, we would recognize the typical X -shaped kernels of the minimax phases SS and its precursors.

Focusing on the boundary kernels computed for the time windows of the SS precursors, we indeed see the typical X -shaped sensitivity kernels predicted for minimax phases (Neele *et al.* 1997; Dahlen 2005; Lawrence & Shearer 2008; Deuss 2009). These boundary sensitivity kernels are shown in Fig. 3. For the time window of the predicted $S\wedge 670S$ (d), the sensitivity is almost

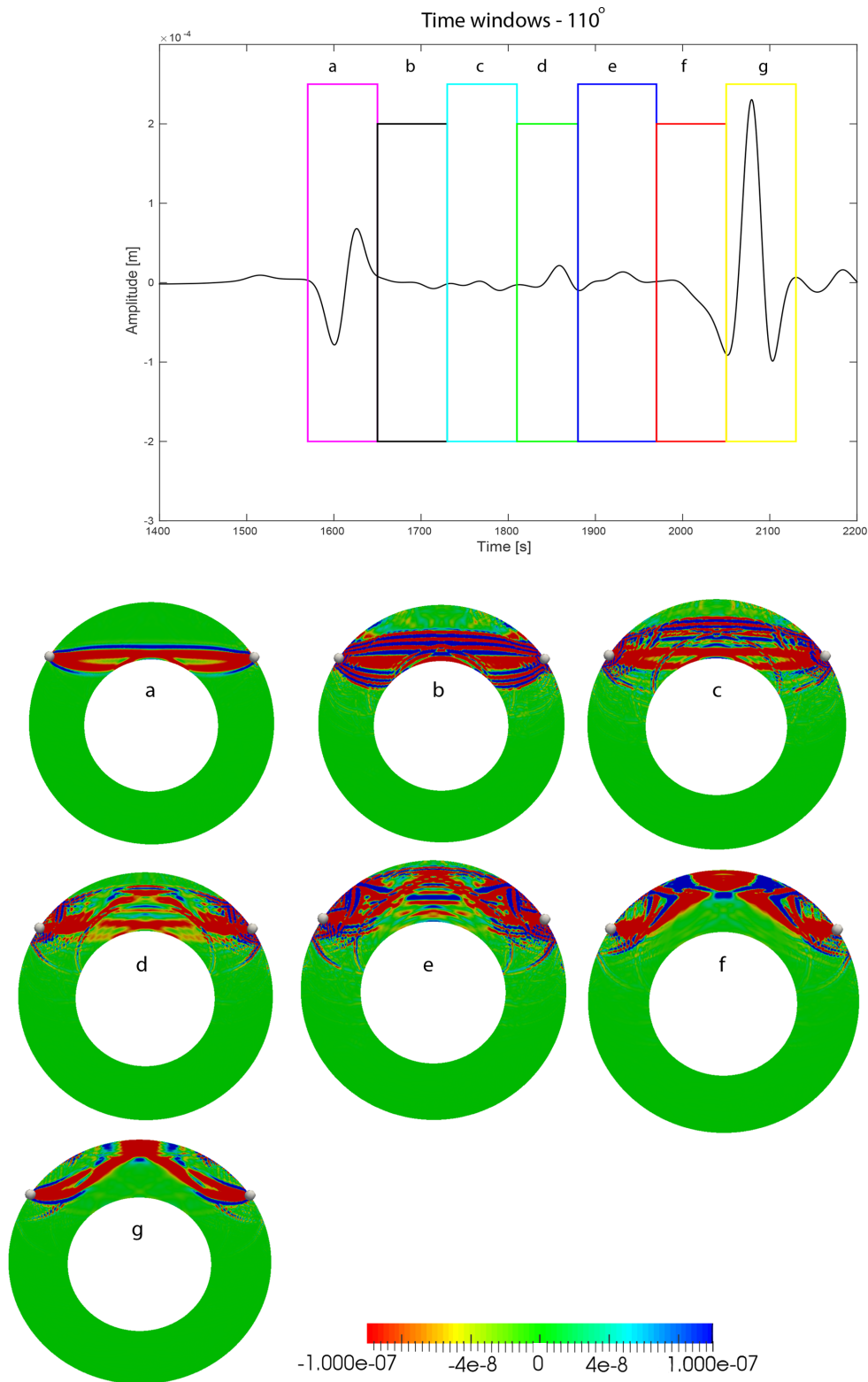


Figure 2. Top panel: the transverse component seismogram with the time windows of the successive kernels corresponds to a station at an epicentral distance of 110.84° . Bottom panel: the volumetric sensitivity kernels for relative shear wave speed variations in background model PREM. The source–receiver locations are shown by the grey spheres. The units are s km^{-3} .

exclusively to the boundary at a depth of 670 km. For the time window (e) of the predicted $S\wedge 400S$, we find an X-shaped sensitivity to the 400 km discontinuity, but also some higher order Fresnel zone sensitivity to the discontinuity at 670 km depth.

3.2 140° distance

The sensitivity kernels for relative changes in V_{SH} are shown in Fig. 4 and the ray theoretical arrivals, calculated by TauP, are shown

Table 1. The time windows shown in Fig. 2 with respect to the centroid source time for the station at an epicentral distance of 110.84° and an event depth of 20 km. In parentheses including the ± 30 s of the source time function. The names of the seismic phases and their traveltimes predicted by PREM within our time windows selections are shown as a guide to understand the volumetric kernels.

Time windows and phase names	Traveltime (PREM)
(a) 1570–1650 s (1540–1680 s)	
<i>SKKS</i>	1565.74 s
<i>SKKKS</i>	1572.49 s
<i>Sdiff</i>	1607.33 s
(b) 1650–1730 s (1620–1760 s)	
<i>S\vee220sSdiff</i>	1703.59 s
(c) 1730–1810 s (1700–1840 s)	
<i>S\vee220sSdiff</i>	1703.59 s
<i>S\vee400sSdiff</i>	1774.59 s
<i>S\vee220sSdiffS\vee220s</i>	1799.85 s
(d) 1810–1880 s (1780–1910 s)	
<i>S\vee220sSdiffS\vee220s</i>	1799.85 s
<i>S\wedge670S</i>	1855.01 s
<i>S\vee670sSdiff</i>	1866.3 s
(e) 1880–1970 s (1850–2000 s)	
<i>S\wedge670S</i>	1855.01 s
<i>S\vee670sSdiff</i>	1866.3 s
<i>S\wedge400S</i>	1930.14 s
<i>S\vee400sSdiffS\vee400s</i>	1941.84 s
(f) 1970–2050 s (1940–2080 s)	
<i>S\vee400sSdiffS\vee400s</i>	1941.84 s
<i>S\wedge220S</i>	1992.17 s
<i>S\vee400sSdiffS\vee670s</i>	2033.56 s
<i>ScS\wedge670ScS</i>	2062.39 s
<i>SS</i>	2078.87 s
(g) 2050–2130 s (2020–2160 s)	
<i>S\vee400sSdiffS\vee670s</i>	2033.56 s
<i>ScS\wedge670ScS</i>	2062.39 s
<i>SS</i>	2078.87 s
<i>S\vee670sSS\vee670s</i>	2125.06 s
<i>ScS\wedge400ScS</i>	2156.67 s

in Table 2. Time window (a) shows a strong sensitivity to S_{diff} in the shape of a banana-doughnut kernel. Jumping to the $S\wedge 670S$ window (b), we observe an underside reflection kernel due to $S\wedge 670S$ and $ScS\wedge 670SKS$. According to the TauP software, the double top-side reflected waves $S\vee 400sSdiffS\vee 400s$ and $S\vee 220sSdiffS\vee 670s$ arrive in this time window too. ScS and various higher order Fresnel zones of S_{diff} interfere, therefore the S_{diff} part of the kernel mostly cancels. The top-side reflections off all the PREM discontinuities interfere but they remain clearly visible. This time window therefore has a complex sensitivity to all upper-mantle discontinuities. There is also sensitivity to a core phase, most likely *SKKKS*. Note that in a spherically symmetric model, although spheroidal and toroidal modes are separated, transverse components show both (e.g. Dahlen & Tromp 1998; Komatitsch & Tromp 2002a). In window (d), we see the $S\wedge 400S$ and the $ScS\wedge 400SKS$ sensitivity, but also a transition zone reverberation of $S\vee 400sSdiffS\vee 670s$ and its symmetric counterpart, again due to the finite source (see Table 2). We can further identify in this time window the underside reflection of

Table 2. Same as in Table 1, now for a station at an epicentral distance of 143.04° and corresponding to the windows shown in Fig. 4.

Time windows and phase names	Traveltime (PREM)
(a) 1850–1890 s (1820–1920 s)	
<i>Sdiff</i>	1876.55 s
(b) 2220–2260 s (2190–2290 s)	
<i>S\vee400sSdiffS\vee400s</i>	2211.05 s
<i>S\vee220sSdiffS\vee670s</i>	2231.77 s
<i>S\wedge670S</i>	2239.70 s
<i>ScS\wedge670SKS</i>	2246.81 s
<i>SKKKS</i>	2250.48 s
(c) 2260–2300 s (2230–2330 s)	
<i>S\vee220sSdiffS\vee670s</i>	2231.77 s
<i>S\wedge670S</i>	2239.70 s
<i>SKS\wedge670ScS</i>	2246.81 s
<i>SKKKS</i>	2250.48 s
<i>SKS\wedge670SKS</i>	2302.51 s
<i>S\vee400sSdiffS\vee670s</i>	2302.77 s
<i>ScS\wedge670ScS</i>	2310.22 s
<i>S\wedge400S</i>	2322.57 s
<i>S\vee670s\wedge400S\vee670s</i>	2322.57 s
(d) 2300–2345 s (2270–2375 s)	
<i>SKS\wedge670SKS</i>	2302.51 s
<i>S\vee400sSdiffS\vee670s</i>	2302.77 s
<i>SKKKS</i>	2304.87 s
<i>ScS\wedge670ScS</i>	2310.22 s
<i>S\wedge400S</i>	2322.57 s
<i>S\vee670s\wedge400S\wedge670S</i>	2322.57 s
<i>ScS\wedge400SKS</i>	2347.43 s
(e) 2455–2500 s (2425–2530 s)	
<i>ScS\wedge220ScS</i>	2474.43 s
<i>SS</i>	2479.52 s

the core phase *SKS \wedge 670SKS*. This time window is therefore sensitive to both, the 400 km and the 670 km discontinuities. Time window (c) between the $S\wedge 670S$ and $S\wedge 400S$ arrivals shows a sensitivity corresponding to an underside reflection, with additional sensitivity covering most parts of the mantle. Arrivals in this time window have sometimes been attributed to a discontinuity around 520 km depth (e.g. Shearer 1990, 1996). PREM, however, has no discontinuity at this depth, despite the corresponding seismogram showing a faint arrival. Bock (1994) already reported such ‘fake’ arrivals due to a model with a simple gradient in the upper-mantle transition zone and the interaction of side-lobes during stacking. We see that this window is within the arrival of $S\vee 400sSdiffS\vee 670s$ and its symmetric counterpart and has a signature of arrivals in windows (b) and (d) due to the finite source in our simulations. Finally, time window (e) shows a strong *SS* wave sensitivity.

The boundary kernels for the precursor time windows (b) and (d) show the expected *X*-shaped sensitivity (Fig. 5). There is clear cross-sensitivity in the sense that the 670-precursor is sensitive to the 400-km discontinuity and vice versa. This contamination stems from the arrivals we identified in the volumetric kernels (see also Table 2).

3.3 160° distance

Fig. 6 shows the volumetric kernels for several time windows for a seismogram recorded at 160° and the corresponding TauP arrivals are given in Table 3. Time window (a) shows a strong S_{diff} sensitivity

Table 3. Same as in Table 1, but now for a station at an epicentral distance of 160.58° and corresponding to the windows shown in Fig. 6.

Time windows and phase names	Traveltime (PREM)
(a) 2000–2040 s (1970–2070 s)	
<i>Sdiff</i>	2023.19 s
<i>SKKS</i>	2046.58 s
(b) 2400–2448 s (2370–2478 s)	
<i>S</i> ∧ <i>670S</i>	2424.71 s
<i>SKS</i> ∧ <i>670SKS</i>	2425.90 s
<i>S</i> ∨ <i>400sSdiff</i> ∨ <i>670s</i>	2449.42 s
<i>ScS</i> ∧ <i>670ScS</i>	2452.55 s
(c) 2448–2488 s (2418–2518 s)	
<i>S</i> ∧ <i>670S</i>	2424.71 s
<i>SKS</i> ∧ <i>670SKS</i>	2425.90 s
<i>S</i> ∨ <i>400sSdiff</i> ∨ <i>670s</i>	2449.42 s
<i>ScS</i> ∧ <i>670ScS</i>	2452.55 s
<i>S</i> ∧ <i>400S</i>	2511.24 s
(d) 2488–2528 s (2458–2558 s)	
<i>S</i> ∧ <i>400S</i>	2511.24 s
<i>SKS</i> ∧ <i>400SKS</i>	2521.36 s
<i>S</i> ∨ <i>670sSdiff</i> ∨ <i>670s</i>	2541.14 s
<i>ScS</i> ∧ <i>400ScS</i>	2544.67 s
(e) 2654–2695 s (2624–2725 s)	
<i>SKS</i> ∧ <i>670SKS</i>	2649.46 s
<i>SS</i>	2672.19 s
<i>SKSSKS</i>	2692.44 s
<i>ScSScS</i>	2712.45 s

and an effect of the *SKKS* core phase due to the 60-s duration of the source time function. Time window (b) is centred around the 670 km precursor and its sensitivity is seen in the kernel. However, there are also (partial) top-side reflections. The ray theoretical calculation identifies the likely candidate as *S*∨*400sSdiff*∨*670s* and its symmetric counterpart. However, because the 400 and 670 km top-side reflections interfere, they are not as strong in the kernel. The core phase is likely the 670 km underside refraction of *SKS*, namely the *SKS*∧*670SKS*, as theoretically predicted. Time window (d) is centred on the 400 km *SS* precursor and the kernel shows sensitivity to *S*∧*400S* but also to the *SKS*∧*400SKS*. The top-side reverberation seen in the kernel is stronger and is the *S*∨*670sSS*∨*670s* due to our source time function of 60 s. Again, window (c) between the main upper-mantle *SS* precursors shows distinct discontinuity arrivals. These are the *ScS*∧*670ScS* and *S*∨*400sSdiff*∨*670s* and their symmetric counterparts. Time window (e) contains the *SS* phase with a very faint signature of core phases.

The boundary kernels for this distance (Fig. 7) exhibit clean, wide *X*-shaped sensitivity to the topography. Although the volumetric shear wave speed kernels show cross-discontinuity sensitivity, the boundary kernels do not in this case.

4 DISCUSSION

4.1 Wave interference

From the observations made on the relative wave speed kernels in the previous section (Figs 2, 4 and 6), we consistently see that *SS* precursors do not arrive in isolation. In each time window, several waves interfere to produce a combined traveltime anomaly. We only showed a few examples, but this observation holds for all long-

period *SS* precursors at other distance ranges. This poses a problem if there is a need to correct the traveltime anomalies for the 3-D velocity structure for inferring boundary topography. This point was already illustrated by Bai *et al.* (2012), who showed that a large amount of the delay times could not be explained by ray theoretical predictions of the arrival times of *SS* precursors, even in a perfectly known 3-D velocity model. The obvious reason for their observation is that the precursors account for only part of the signal in the precursor time windows. Since they did not account for the interference with the other arrivals, their predicted traveltime variations were off by 50 per cent from their measurements. Sometimes ray theory is blamed for the shortcomings in predicting delay times and banana-doughnut kernels are advocated (e.g. Zhao & Chevrot 2003; Bai *et al.* 2012), but theoretical sensitivity kernels for isolated seismic phases as those in Zhao & Chevrot (2003), for instance, will not solve the problem of interfering phases. Full sensitivity kernels, like the ones we showed above, are needed to account for the effect of many phases contributing to the delay times.

We would like to note that our long STF is not the reason for this observed interference, although, because of the extended STF, some extra phases might contribute. It is also worth noting that the kernels will not be substantially different because of the implemented STF, only smoothed. We checked that kernels for Green's functions contained essentially the same information. A last point is that the kernel does not always show all the phases predicted by ray theory. This is mainly due to the focal mechanism, which has a profound effect on the kernel (e.g. Sieminski *et al.* 2009). It is important to realize that our kernels are exact for a given Earth model, focal mechanism and STF.

4.2 Boundary topography and/or 3-D velocity structure?

Ultimately, whether the multiple arrivals are a problem for the 3-D velocity corrections will depend on the relative importance of the contributions from the topographic and the 3-D velocity structure to the measured traveltime shift δt . To investigate this, we used the synthetic data calculated in Koroni & Trampert (2016) using the models PREM, PREM+TOPO, S20RTS and S20RTS+TOPO, where TOPO stands for the topography models of the 400 and 670 km discontinuities from Meier *et al.* (2009) scaled to ± 30 km. We plotted histograms of the time residuals measured by cross-correlating seismograms in selected precursor time windows. More specifically, the time windows are centred around the *S*∧*400S* and *S*∧*670S* arrivals calculated in PREM using TauP (Crotwell *et al.* 1999). The time windows have a width of 80 s and the measured delay time (δt) corresponds to the maximum of the cross-correlation. The effect of 3-D velocity structure is measured by cross-correlating the seismograms in S20RTS with those in PREM to give:

$$\delta t^{S20RTS-PREM} = t^{S20RTS} - t^{PREM} \quad (3)$$

where t is the traveltime of the precursor in the given model shown by the superscript. To estimate the contribution from the topography model alone we define:

$$\delta t^{[PREM+TOPO]-PREM} = t^{[PREM+TOPO]} - t^{PREM} \quad (4)$$

for a 1-D velocity background model, and:

$$\delta t^{[S20RTS+TOPO]-S20RTS} = t^{[S20RTS+TOPO]} - t^{S20RTS} \quad (5)$$

for the 3-D velocity background model. The results are shown in Fig. 8 where histograms of δt defined above are plotted for the two time windows corresponding to *S*∧*400S* and *S*∧*670S*. For the

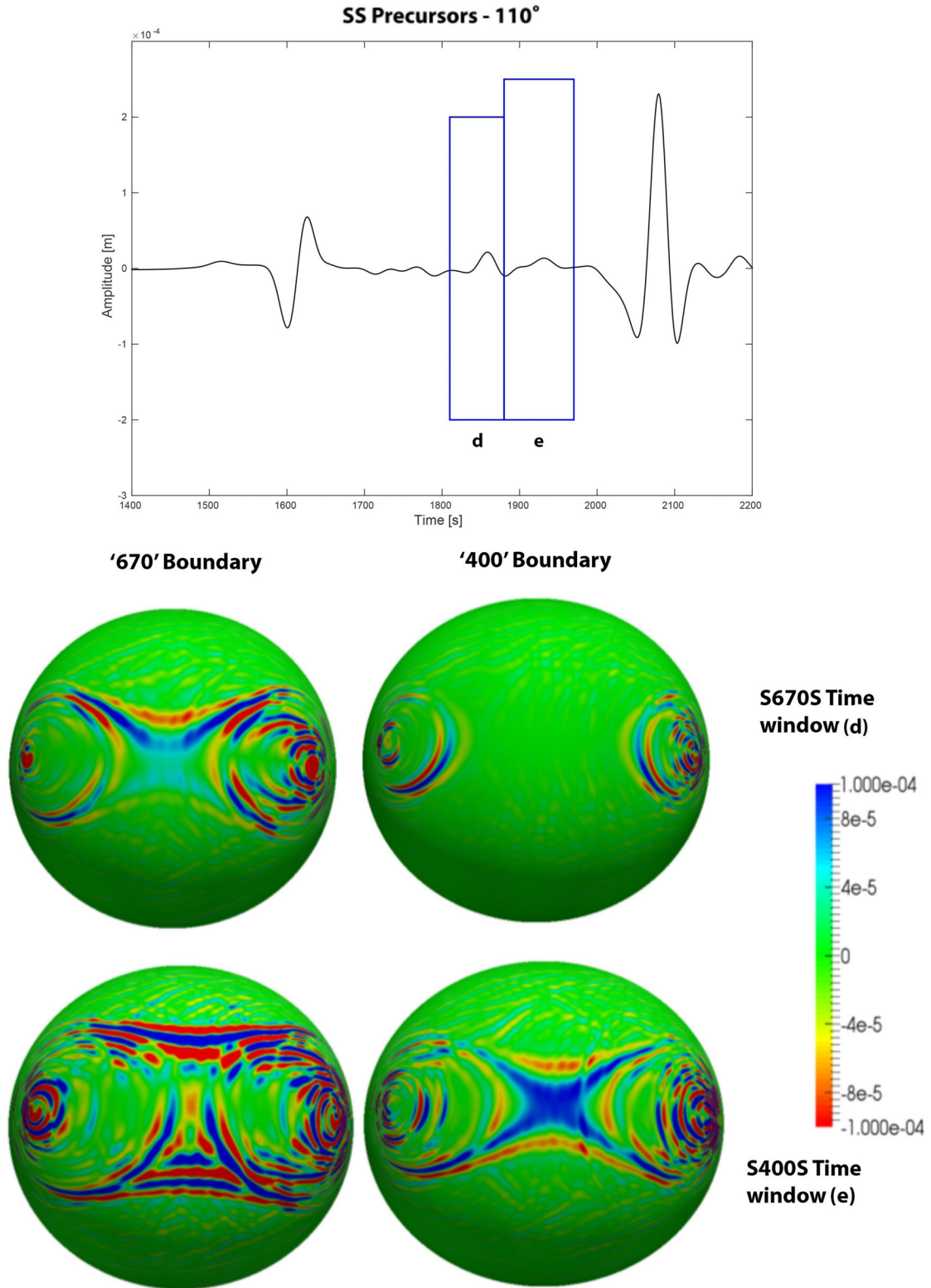


Figure 3. Top panel: the transverse component seismogram calculated for background model PREM and the time windows around the predicted *SS* precursors arrivals. Bottom panel: boundary kernels for the time windows corresponding to the *SS* precursors. The sensitivity to the boundary topography is shown. The units for the boundary kernels are s km^{-2} .

topography models used in our simulations, we observe that the 3-D velocity contributions are of the same order but slightly larger than those from the topography. Unless for the real earth the 3-D velocity perturbations are much smaller or the discontinuity topography

variations much larger, it appears, given the multiple arrivals and their interference in each time window, that it will be difficult to make accurate corrections for the 3-D velocity structure in order to retrieve discontinuity topography.

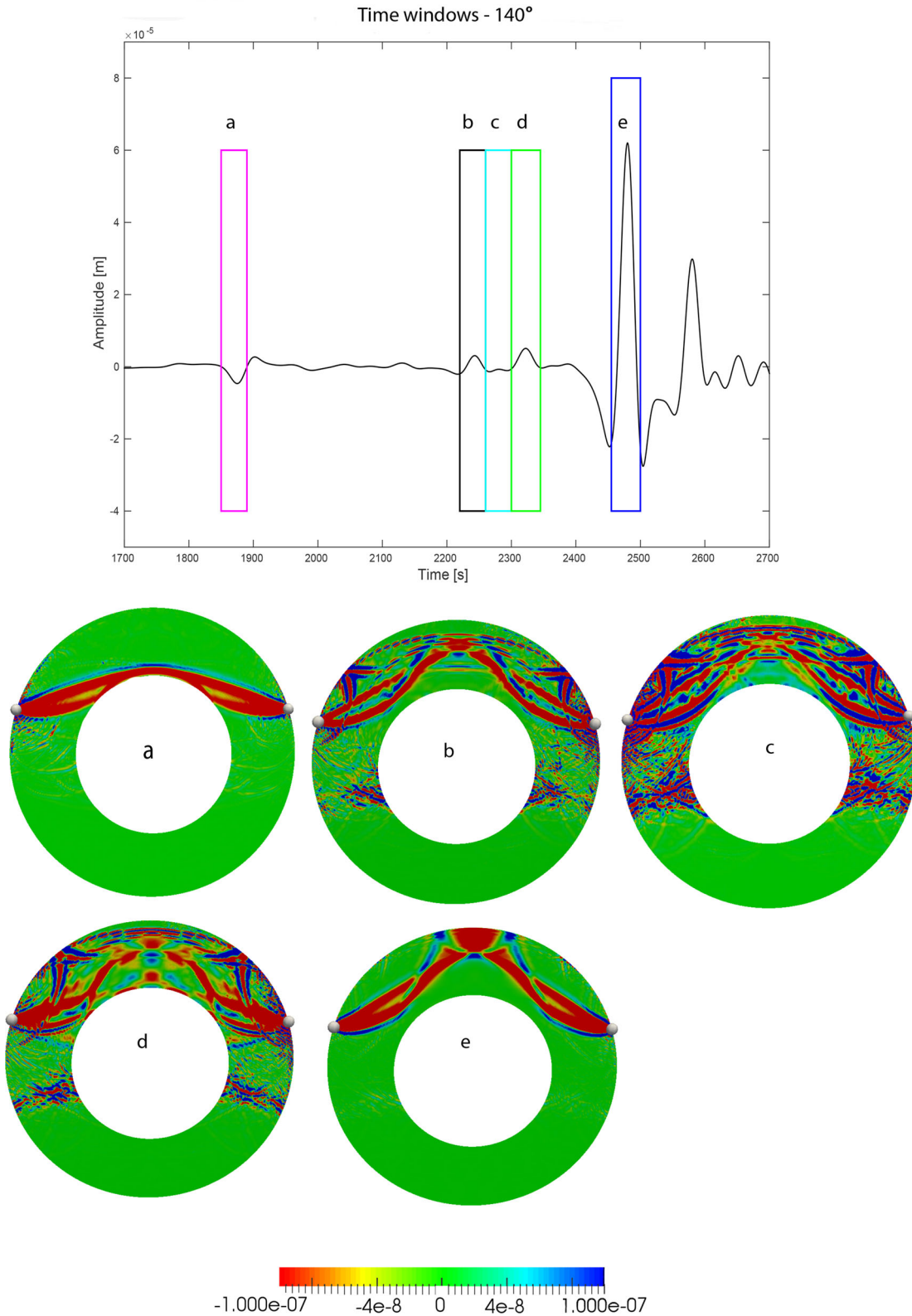


Figure 4. Same as Fig. 2, but now for the receiver at an epicentral distance of 143.04°.

A more fundamental problem was recently identified by Koroni & Trampert (2016). They showed that the delay times of *SS* precursors caused by topographic variations and by 3-D velocity structure are not additive in the sense that:

$$\begin{aligned}
 t^{[S20RTS+TOPO]} - t^{PREM} &\neq \underbrace{t^{[S20RTS+TOPO]} - t^{S20RTS}}_{\text{=time delay due to topographic variation}} \\
 &+ \underbrace{t^{S20RTS} - t^{PREM}}_{\text{=time delay due to 3-D velocity structure}} \quad (6)
 \end{aligned}$$

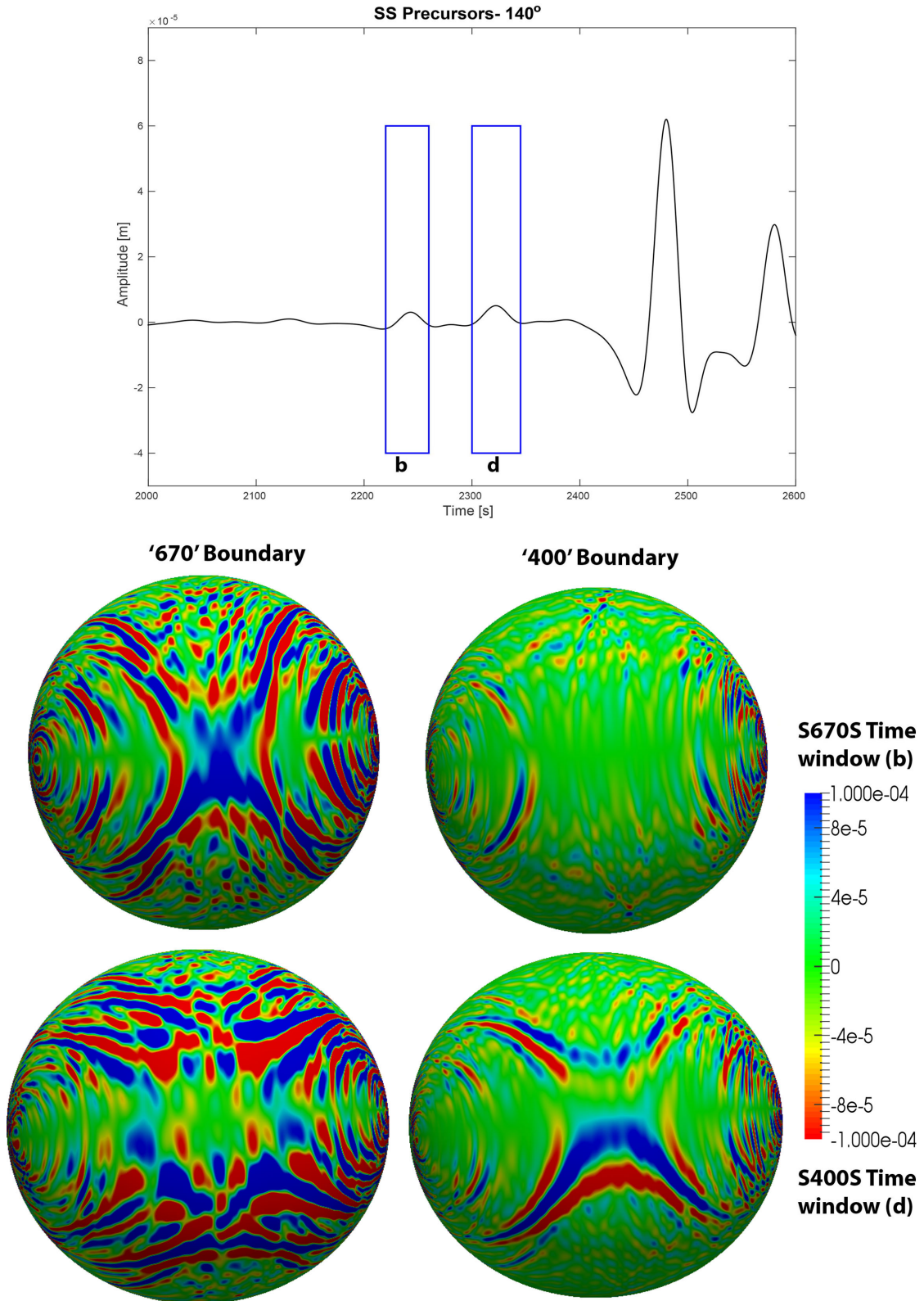


Figure 5. Same as Fig. 3, but now for the receiver at an epicentral distance of 143.04°.

or using expressions (3)–(5):

$$\delta t^{[S20RTS+TOPO]-PREM} \neq \delta t^{[S20RTS+TOPO]-S20RTS} + \delta t^{S20RTS-PREM} \quad (7)$$

To first order these delay times can be expressed using Fréchet derivatives of traveltimes in the appropriate background models (see eqs 1 and 2). If this linearizing assumption captures most of the physics, the following expressions should

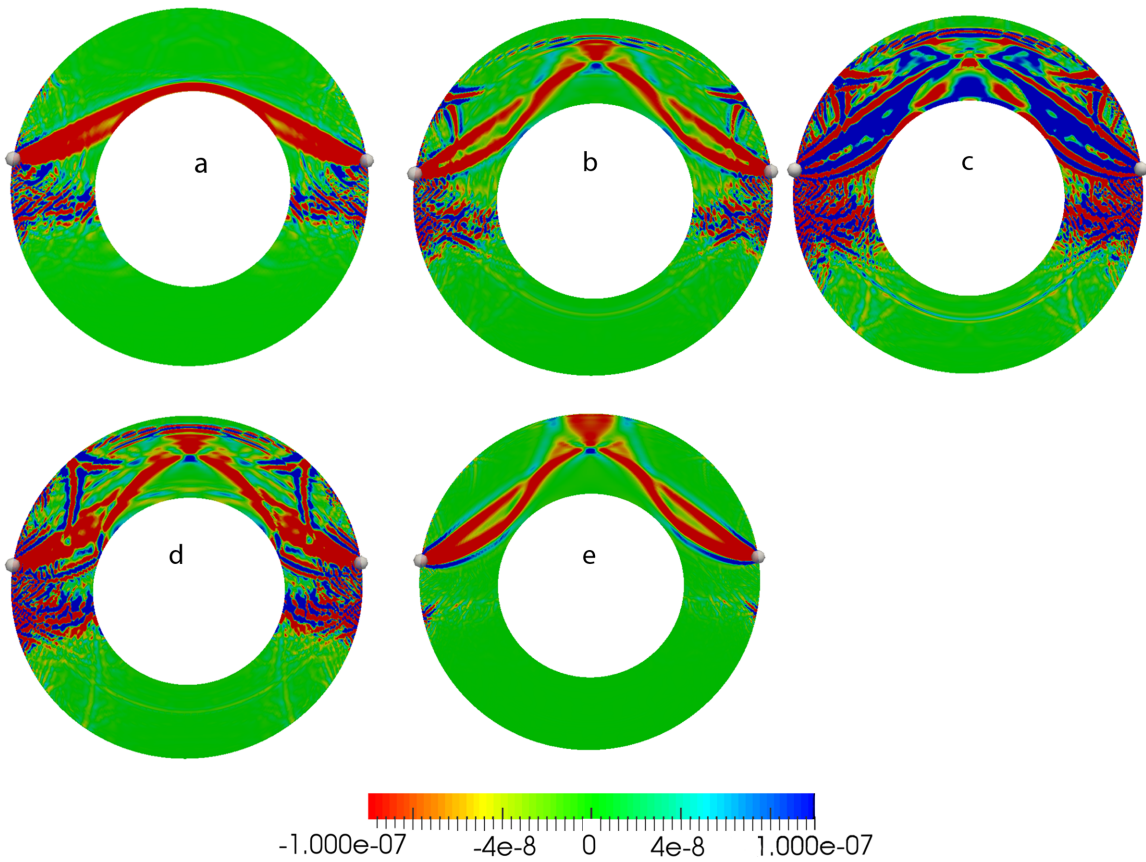
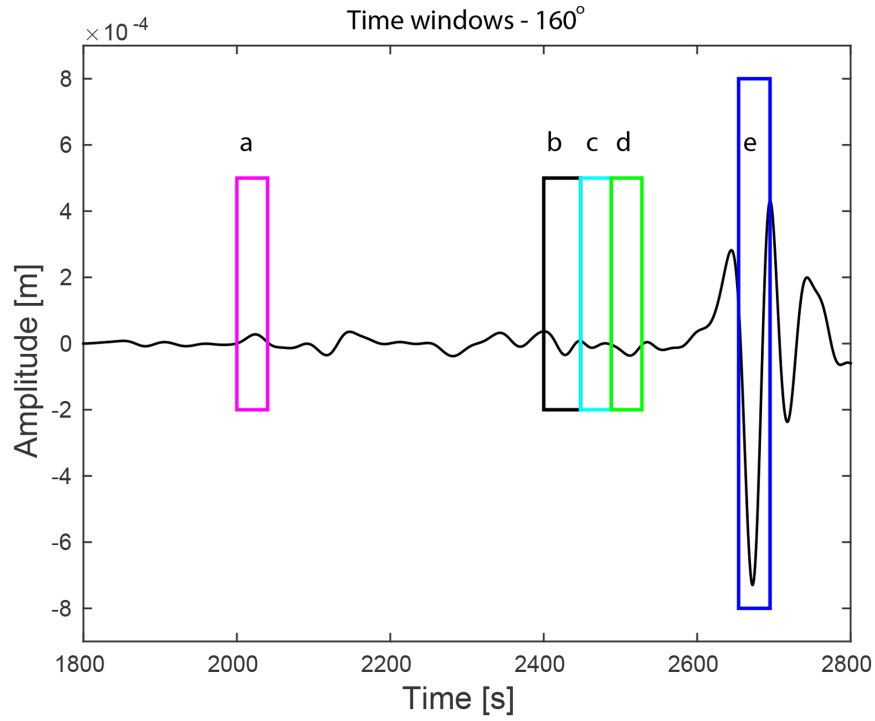


Figure 6. Same as Fig. 2, but now for the receiver at an epicentral distance of 160.58° .

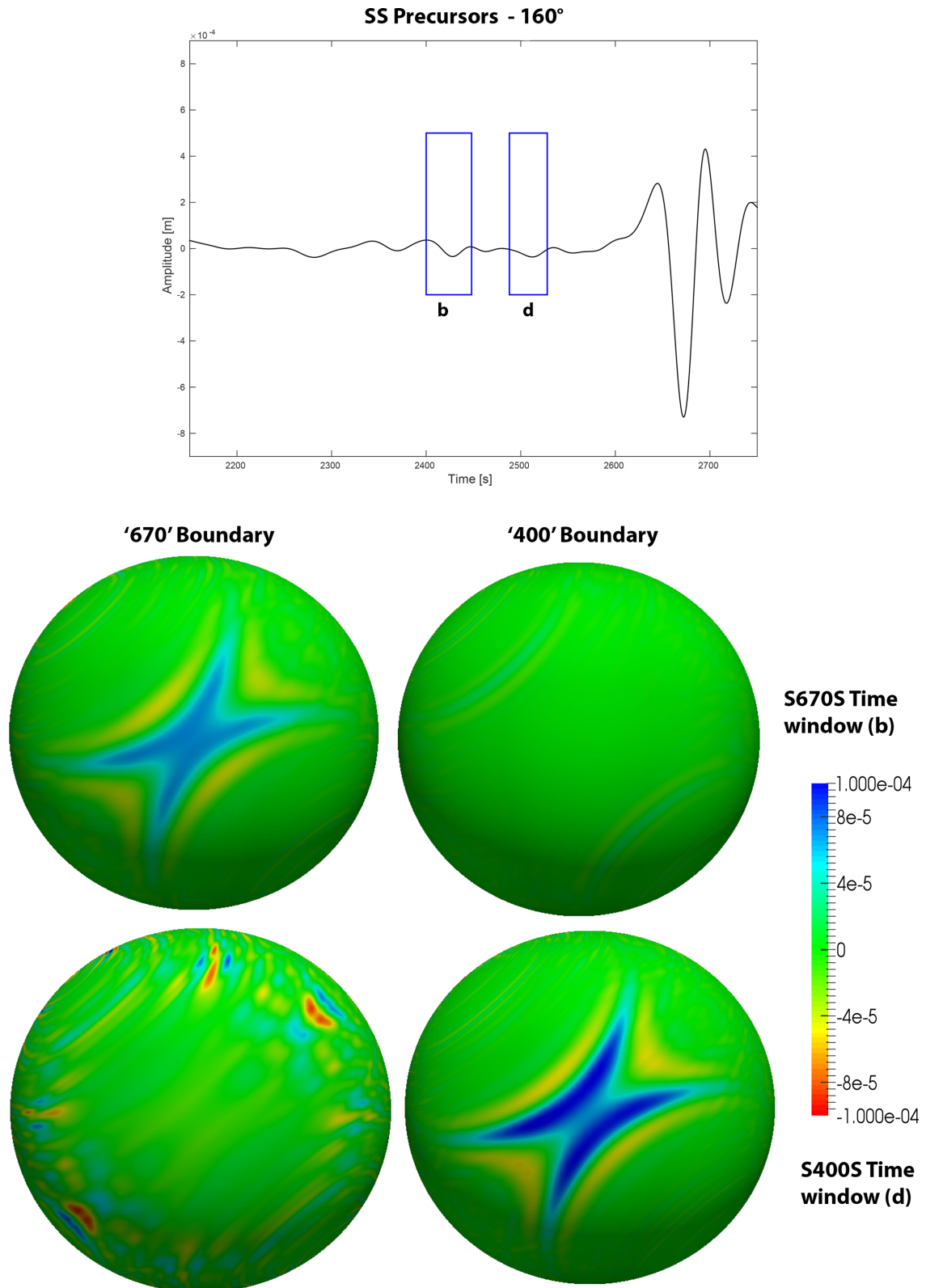


Figure 7. Same as Fig. 3, but now for the receiver at an epicentral distance of 160.58°.

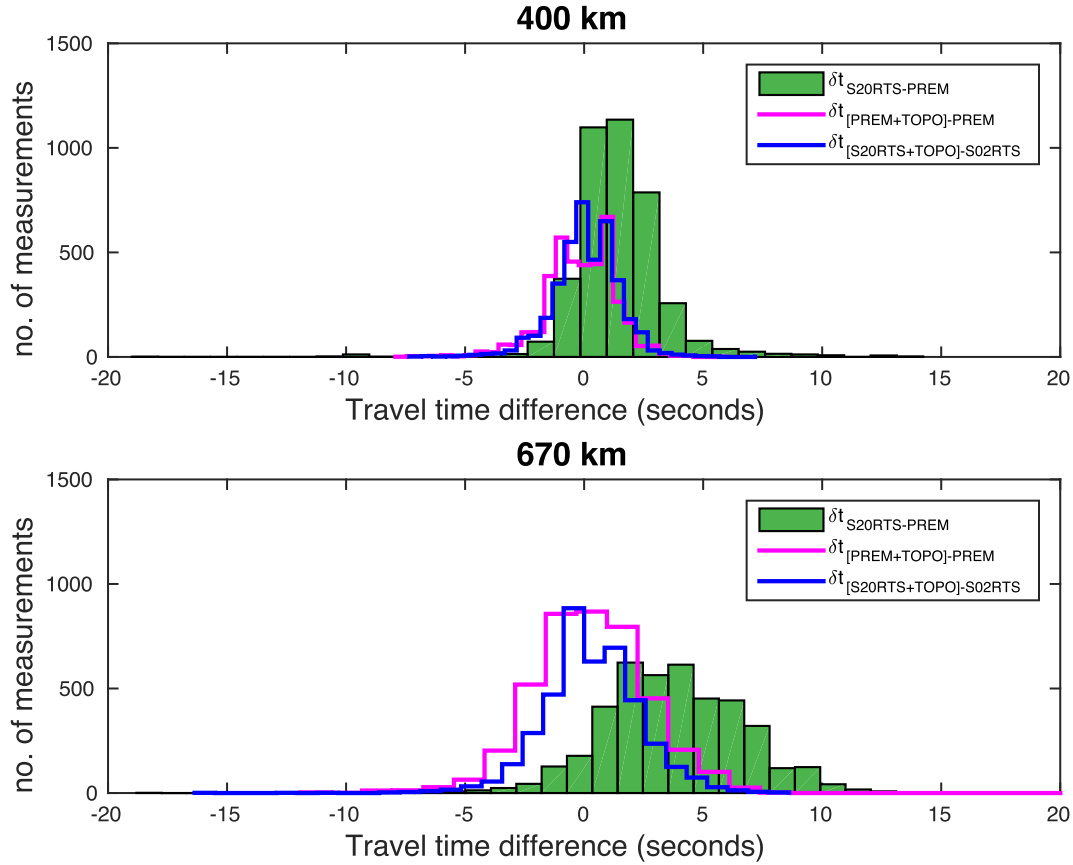


Figure 8. Histograms showing the distribution of traveltimes delays caused by the relative perturbation in 3-D shear velocity (green bars) and those caused by topography in upper-mantle discontinuities in PREM (magenta line) and in S20RTS as background model (purple line). These time delays are measured by windowing around the PREM arrival of the $S^{\wedge}400S$ (top panel) and $S^{\wedge}670S$ (bottom panel) precursors.

hold:

$$\begin{aligned}
 \delta t^{[S20RTS+TOPO]-PREM} &= \int K_V^{PREM} d \ln V_{SH} dx^3 \\
 &\quad + \int K_r^{PREM} d \ln r dx^2 \\
 \delta t^{[S20RTS+TOPO]-S20RTS} &= \int K_r^{S20RTS} d \ln r dx^2 \\
 \delta t^{S20RTS-PREM} &= \int K_V^{PREM} d \ln V_{SH} dx^3
 \end{aligned} \quad (8)$$

where δt is again the traveltime delay and the superscripts in the kernels (K) specify the background models in which they should be calculated. Inserting these expressions into eq. (7) we should find that

$$\int K_r^{PREM} d \ln r dx^2 \neq \int K_r^{S20RTS} d \ln r dx^2. \quad (9)$$

To check how far the inequality in expression (9) holds, we show in Fig. 9 the boundary kernels together with our sample seismogram at a distance of 143.04° , in a 1-D and 3-D background velocity model (PREM and S20RTS, respectively). The time windows used to compute the boundary kernels are selected based on the predicted arrival of the SS precursors in PREM. Although the arrival times of these seismic phases slightly differ in a 3-D model, the width of the time windows is sufficiently large to capture the energy of the SS precursors, in both the 1-D and 3-D background models (see Fig. 9 top panel). We observe that the boundary kernels indeed differ

significantly. For the 400 km boundary, the kernels have the same magnitude but the characteristic X -shapes are slightly misplaced. Because these shapes are narrow and elongated, their integrated contribution to the delay time will be significantly different. For the 670 km boundary, the kernels in this example have largely different amplitudes depending on the background model. These kernels demonstrate that the boundary sensitivity changes a lot with the background model. In particular, the kernel is almost 5 times larger in the 3-D background model. This can easily be understood as the waveform in the 3-D background model contains more energy than that in the 1-D background model (Fig. 9 top panel, window b). This means that the delay times caused by boundary topography and by 3-D velocity structure cannot be separated into two independent contributions. This effect was measured by Koroni & Trampert (2016) for all events and station configurations in their synthetic experiment. This non-linearity has nothing to do with imperfect shear velocity corrections, but with the strong change of boundary kernels with the background model. We speculate that this significant change in kernels is because of the X -shaped nature of the boundary kernel of the minimax phase. For minimum traveltime phases, the boundary sensitivity kernels are elliptic and there is therefore a higher chance of more overlap with changing background models. This is seen by Rutten (2017), who used synthetic seismograms in a model with CMB topography and measured traveltime differences due to CMB topography on seismic phases such as PcP , ScS , ScP , which are minimum traveltime phases. Following a similar process as Koroni & Trampert (2016), she found that these traveltimes were additive.

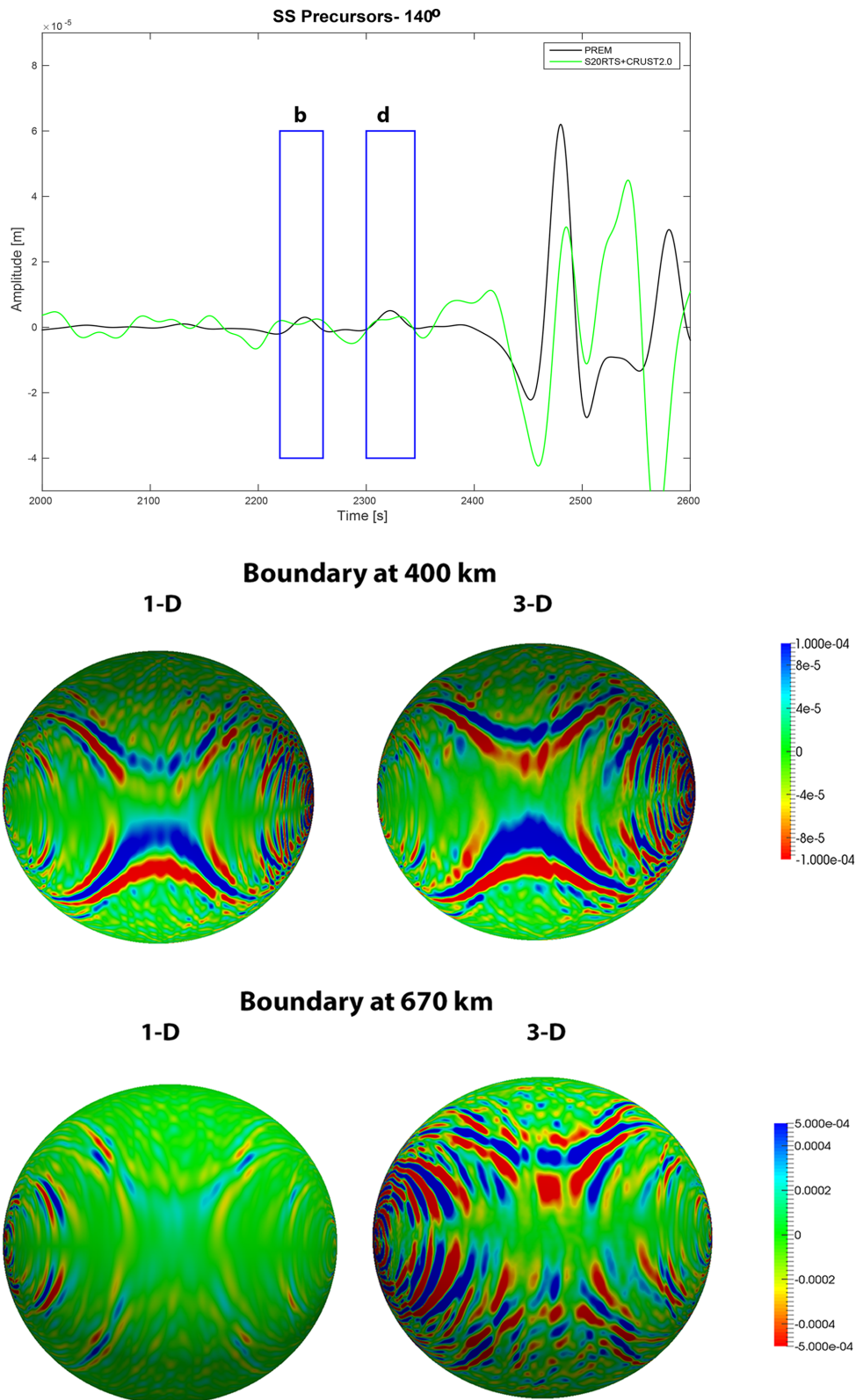


Figure 9. Top panel: the waveforms in the 1-D and 3-D background model are shown along with the selected time windows b and d, which correspond to the predicted arrivals of $S^{\wedge}400S$ and $S^{\wedge}670S$ in PREM. Boundary kernels for SS precursors in 1-D and 3-D background models: The $S^{\wedge}400S$ kernel (middle panel) and $S^{\wedge}670S$ kernel (bottom panel) are shown at different scales since we do not seek to compare them to each other, but rather to compare the 1-D to 3-D difference.

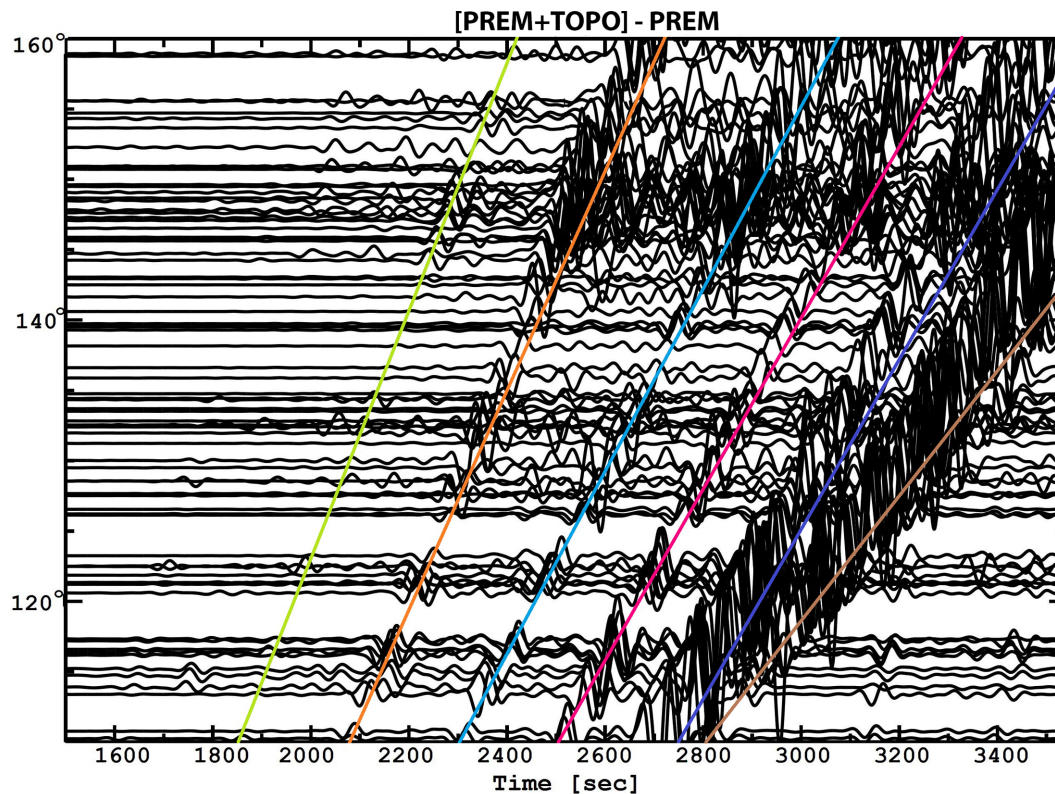


Figure 10. Traveltime curve of differences between seismograms in PREM and PREM+TOPO. The green line corresponds to S^{670S} , the orange line to SS , the cyan line to SSS , the magenta line to $SSSS$, the blue line to $SSSSS$ and the brown line to $SSSSSS$ arrival times in PREM.

Note that most studies in fact use differential traveltimes with respect to SS . Transforming the traveltime anomaly δt in eqs (7) and (8) into Δt by

$$\Delta t = \delta t_{\text{precursor}} - \delta t_{SS} \quad (10)$$

the kernels in eqs (8) and (9) then need to be replaced by:

$$\Delta K = K_{\text{precursor}} - K_{SS}. \quad (11)$$

All our arguments as well as the conclusions on additivity remain unchanged as there is no prospect of eq. (9) being violated.

By analysing our synthetic seismograms, we further noted that other parts show significantly more sensitivity to topography than the precursory wavefield. In particular, the multiples of the S wave, namely SSS , $SSSS$, $SSSSS$ and $SSSSSS$ express a high sensitivity to changes in the topographic structure at the 400 and 670 km boundaries. This is a consistent observation and to provide evidence, we plotted the difference of the seismograms calculated in PREM and in PREM+TOPO as a function of epicentral distance, which is shown in Fig. 10. The difference plots indicate that there are portions in the transverse component seismograms which are far more informative regarding the topographic structure of the 400 and 670 km discontinuities than the part corresponding to the SS precursors. These places of high sensitivity correspond to arrivals of multiples of S waves and are likely due to triplication in the traveltime curves caused by interaction with the upper-mantle discontinuities. The sensitivity of these phases to upper-mantle structure is well-known and has been investigated in waveform modelling studies (e.g. Grand & Helmberger 1984; Tan & Helmberger 2007; Staelher *et al.* 2012). The multiples of the S wave are also taken into account in inversions for mantle structure using adjoint methods (e.g. Bozdogan *et al.* 2016). However, this type of data has to date not

been used for inferring the global topographic variations of upper-mantle discontinuities. One likely reason is the observed trade-off between shear wave speed and topographic structure (e.g. Chaljub & Tarantola 1997; Shearer 2000; Gu & Dziewonski 2002; Song *et al.* 2004) which may indeed hamper the inference of global topography maps of the ‘400’ and ‘670’ discontinuities. To deal with the problem of trade-off, some studies have performed joint inversions of shear wave speed and topographic structure (e.g. Gu *et al.* 2003; Houser *et al.* 2008) using mainly traveltime of SS precursors and ray theory. Based on the analyses above, we suggest that only a full waveform inversion for both shear wave speed and topographic structure using accurate forward models and exact Fréchet kernels will enable us to image the upper-mantle discontinuities. Such a full waveform imaging will clearly benefit from including multiply bouncing S waves.

5 CONCLUDING REMARKS

Taking into account the evidence seen on the volumetric and boundary sensitivity kernels, we can summarize the following points:

(i) Long-period SS precursors never arrive isolated in a long-period time window for the 110° – 160° distance range investigated here. Therefore, it is impossible to make adequate 3-D velocity corrections of delay times of SS precursors, ray theory or other, unless one knows all the phases which arrive in the chosen time window.

(ii) The effect of the 3-D velocity structure and the topography on the delay times of SS precursors is likely to be of similar size and thus both effects are not easily distinguishable.

(iii) The X -shaped boundary kernels of SS precursors change significantly with the background model in which they are calculated. Therefore, the contributions of the 3-D velocity structure and the boundary topography are not additive in the delay time.

(iv) Other time windows than those of SS precursors exhibit much more sensitivity to the topography of upper-mantle discontinuities, especially those involving the triplications of multiples of the S wave. Given that these waves have not been explicitly used to map the '400' and '670' topography globally, we suggest that they should be used in a full waveform approach.

Because of the points made above, it seems impossible to infer boundary topography from delay times of SS precursors based on ray theoretical concepts. We suggest that a full waveform approach is essential to globally map upper-mantle discontinuities and that the 3-D mantle velocity and boundary structure of internal discontinuities should be inferred simultaneously.

ACKNOWLEDGEMENTS

We would like to thank the editor Dr Ana Ferreira, Li Zhao and an anonymous reviewer for constructive comments and suggestions. We also thank Theo van Zessen for maintaining our local cluster. The data used in this study are available via http://www.geo.uu.nl/~jeannot/My_web_pages/Downloads.html. The figures were created using the GMT Software (Wessel *et al.* 2013) and ParaView (Ayachit 2015). The research leading to these results has received funding from the European Research Council under the European Union's Seventh Framework Programme (FP/2007-2013)/ERC Grant Agreement Number 320639 (iGEO).

REFERENCES

- Ayachit, U., 2015. *The ParaView Guide: A Parallel Visualization Application*, Kitware.
- Bai, L., Zhang, Y. & Ritsema, J., 2012. An analysis of SS precursors using spectral-element method seismograms, *Geophys. J. Int.*, **188**, 293–300.
- Bassin, C., Laske, G. & Masters, G., 2000. The current limits of resolution for surface wave tomography in North America, *EOS, Trans. Am. geophys. Un.*, **81**, F897.
- Bock, G., 1994. Synthetic seismogram images of upper mantle structure: no evidence for a 520-km discontinuity, *J. geophys. Res.*, **99**(B8), 15 843–15 851.
- Bozdag, E., Peter, D., Komatitsch, M.L.D., Tromp, J., Hill, J., Podhorszki, N. & Pugmire, D., 2016. Global adjoint tomography: first-generation model, *Geophys. J. Int.*, **207**, 1739–1766.
- Chaljub, E. & Tarantola, A., 1997. Sensitivity of SS precursors to topography on the upper-mantle 660-km discontinuity, *Geophys. Res. Lett.*, **24**(21), 2613–2616.
- Chambers, K., Woodhouse, J.H. & Deuss, A., 2005. Topography of the 410-km discontinuity from PP and SS precursors, *Earth planet. Sci. Lett.*, **235**, 610–622.
- Crotwell, H.P., Owens, T.J. & Ritsema, J., 1999. The TauP Toolkit: flexible seismic travel-time and raypath utilities, *Seismol. Res. Lett.*, **70**, 154–160.
- Dahlen, F.A., 2005. Finite-frequency sensitivity kernels for boundary topography perturbations, *Geophys. J. Int.*, **162**, 525–540.
- Dahlen, F.A. & Tromp, J., 1998. *Theoretical Global Seismology*, Princeton Univ. Press.
- Dahlen, F., Hung, S.-H. & Nolet, G., 2000. Fréchet kernels for finite frequency traveltimes – I. theory, *Geophys. J. Int.*, **141**, 157–174.
- Deuss, A., 2009. Global observations of mantle discontinuities using SS and PP precursors, *Surv. Geophys.*, **30**, 301–326.
- Dziewoński, A.M. & Anderson, D.L., 1981. Preliminary reference Earth model, *Phys. Earth planet. Inter.*, **25**, 297–356.
- Ekström, G., Nettles, M. & Dziewoński, A.M., 2012. The global CMT project 2004–2010: centroid-moment tensors for 13,017 earthquakes, *Phys. Earth planet. Inter.*, **200–201**, 1–9.
- Flanagan, M. & Shearer, P., 1998. Global mapping of topography on transition zone velocity discontinuities by stacking SS precursors, *J. geophys. Res.*, **103**, 2673–2692.
- Flanagan, M. & Shearer, P., 1999. A map of topography of 410-km discontinuity from PP precursors, *Geophys. Res. Lett.*, **26**(5), 549–552.
- Gauthier, O., Virieux, J. & Tarantola, A., 1986. Two-dimensional non-linear inversion of seismic waveforms: numerical results, *Geophysics*, **51**, 1387–1403.
- Grand, S. & Helmberger, D.V., 1984. Upper mantle shear structure beneath the Northwest Atlantic Ocean, *J. geophys. Res.*, **89**(B13), 11 465–11 475.
- Gu, Y.J. & Dziewoński, A.M., 1998. Global de-correlation of the topography of transition zone discontinuities, *Earth planet. Sci. Lett.*, **157**, 57–67.
- Gu, Y.J. & Dziewoński, A.M., 2002. Global variability of transition zone thickness, *J. geophys. Res.*, **107**(B7), ESE 2-1ESE 2-17.
- Gu, Y.J., Dziewoński, A.M. & Ekstrom, G., 2003. Simultaneous inversion for mantle shear velocity and topography of transition zone discontinuities, *Geophys. J. Int.*, **154**, 559–583.
- Helfrich, G., 1999. Thermal variations in the mantle inferred from 660 km discontinuity topography and tomographic wave speed variations, *Geophys. J. Int.*, **151**(3), 935–943.
- Houser, C., Masters, G., Flanagan, M. & Shearer, P., 2008. Determination and analysis of long-wavelength transition zone structure using SS precursors, *Geophys. J. Int.*, **174**, 178–194.
- Johnson, L.R., 1967. Array measurements of P velocities in the upper mantle, *J. geophys. Res.*, **72**(24), 6039–6325.
- Komatitsch, D. & Tromp, J., 1999. Introduction to the spectral element method for three-dimensional seismic wave propagation, *Geophys. J. Int.*, **139**(3), 806–822.
- Komatitsch, D. & Tromp, J., 2002a. Spectral-element simulations of global seismic wave propagation – I. Validation, *Geophys. J. Int.*, **149**(2), 390–412.
- Komatitsch, D. & Tromp, J., 2002b. Spectral-element simulations of global seismic wave propagation – II. 3-D models, oceans, rotation, and self-gravitation, *Geophys. J. Int.*, **150**(1), 303–318.
- Komatitsch, D. & Vilotte, J.P., 1998. The spectral-element method: an efficient tool to simulate the seismic response of 2D and 3D geological structures, *Bull. seism. Soc. Am.*, **88**(2), 368–392.
- Koroni, M. & Trampert, J., 2016. The effect of topography of upper mantle discontinuities on SS precursors, *Geophys. J. Int.*, **204**, 667–681.
- Lawrence, J.F. & Shearer, P.M., 2008. Imaging mantle transition zone thickness with SdS - SS finite-frequency sensitivity kernels, *Geophys. J. Int.*, **174**, 143–158.
- Liu, Q. & Tromp, J., 2006. Finite-frequency kernels based on adjoint methods, *Bull. seism. Soc. Am.*, **96**(6), 2383–2397.
- Liu, Q. & Tromp, J., 2008. Finite-frequency sensitivity kernels for global seismic wave propagation based upon adjoint methods, *Geophys. J. Int.*, **174**(1), 265–286.
- Luo, Y. & Schuster, G., 1991. Wave-equation traveltimes inversion, *Geophys.*, **56**, 645–653.
- Marquering, H., Nolet, G. & Dahlen, F., 1999. Three-dimensional sensitivity kernels for finite-frequency traveltimes: the banana-doughnut paradox, *Geophys. J. Int.*, **137**, 805–815.
- Meier, U., Trampert, J. & Curtis, A., 2009. Global variations of temperature and water content in the mantle transition zone from higher mode surface waves, *Earth planet. Sci. Lett.*, **282**, 91–101.
- Neele, F., de Regt, H. & VanDecar, J., 1997. Gross errors in upper-mantle discontinuity topography from underside reflection data, *Geophys. J. Int.*, **129**, 194–204.
- Niazi, M. & Anderson, D.L., 1965. Upper mantle structure of western North America from apparent velocities of P waves, *J. geophys. Res.*, **70**, 4633–4640.
- Revenaugh, J. & Jordan, T., 1991. Mantle layering from ScS reverberations, *J. geophys. Res.*, **96**(B12), 19 781–19 810.

- Ritsema, J., Van Heijst, H.J. & Woodhouse, J.H., 1999. Complex shear velocity structure imaged beneath Africa and Iceland, *Science*, **286**, 1925–1928.
- Rondenay, S., 2009. Upper mantle imaging with array recordings of converted and scattered teleseismic waves, *Surv. Geophys.*, **30**, 377–405.
- Rutten, L., 2017. Synthetic modelling of core-mantle boundary topography, *UU Theses Archive*, <https://dspace.library.uu.nl/handle/1874/344196>.
- Schmerr, N. & Garnero, E., 2006. Investigation of upper mantle discontinuity structure beneath the central Pacific using *SS* precursors, *J. geophys. Res.*, **111**, B08305, doi:10.1029/2005JB004197.
- Shearer, P.M., 1990. Seismic imaging of upper mantle structure and new evidence for a 520 km discontinuity, *Nature*, **344**, 121–126.
- Shearer, P.M., 1991. Constraints on upper mantle discontinuities from observations of long-period reflected and converted phases, *J. geophys. Res.*, **96**, 18 147–18 182.
- Shearer, P., 1993. Global mapping of upper mantle reflectors from long-period *SS* precursors, *Geophys. J. Int.*, **115**, 878–904.
- Shearer, P.M., 1996. Transition zone velocity gradients and the 520-km discontinuity, *J. geophys. Res.*, **101**, 3053–3066.
- Shearer, P.M., 2000. Upper mantle seismic discontinuities, in *Earth's Deep Interior: Mineral Physics and Tomography from the Atomic to the Global Scale*, Geophysical Monograph, vol. 117, pp. 115–131, American Geophysical Union.
- Shearer, P. & Masters, G., 1992. Global mapping of topography on 660-km discontinuity, *Nature*, **355**, 791–796.
- Sieminski, A., Trampert, J. & Tromp, J., 2009. Principal component analysis of anisotropic finite-frequency sensitivity kernel, *Geophys. J. Int.*, **179**, 1186–1198.
- Song, T.-R.A., Helmberger, D. & Grand, S., 2004. Low-velocity zone atop the 410-km seismic discontinuity in the northwestern United States, *Nature*, **427**, 530–533.
- Staelher, S.C., Sigloch, K. & Nissen-Meyer, T., 2012. Triplicated *P*-wave measurements for waveform tomography of the mantle transition zone, *Solid Earth*, **3**, 339–354.
- Talagrand, O. & Courtier, P., 1987. Variational assimilation of meteorological observations with the adjoint vorticity equation. I: Theory, *Q. J. R. Meteorol. Soc.*, **113**, 1311–1328.
- Tan, Y. & Helmberger, D.V., 2007. Trans-Pacific upper mantle shear velocity structure, *J. geophys. Res.*, **112**, B08301, doi:10.1029/2006JB004853.
- Tarantola, A., 1984. Inversion of seismic reflection data in the acoustic approximation, *Geophysics*, **49**, 1259–1266.
- Tarantola, A., 1988. Theoretical background for the inversion of seismic waveforms, including elasticity and attenuation, *Pure appl. Geophys.*, **128**, 365–399.
- Tromp, J., Tape, C. & Liu, Q., 2005. Seismic tomography, adjoint methods, time reversal and banana-doughnut kernels, *Geophys. J. Int.*, **160**(1), 195–216.
- Vinnik, L.P., 1977. Detection of waves converted from *P* to *SV* in the mantle, *Phys. Earth planet. Inter.*, **15**, 39–45.
- Wessel, P., Smith, W. H.F., Scharroo, R., Luis, J. & Wobbe, F., 2013. Generic mapping tools: improved version released, *EOS, Trans. Am. geophys. Un.*, **94**(45), 409–410.
- Zhao, L. & Chevrot, S., 2003. *SS*-wave sensitivity to upper mantle structure: implications for the mapping of transition zone discontinuity topographies, *Geophys. Res. Lett.*, **30**(11), 1590, doi:10.1029/2003GL017223.
- Zhao, L.-S. & Helmberger, D.V., 1993. Upper mantle compressional velocity structure beneath the northwest atlantic ocean, *J. geophys. Res.*, **98**(B8), 14 185–14 196.